Performance Analysis of a Dual-Inverter-Fed Open-End Winding Induction Machine under Asymmetrical Control: Theoretical Approach and Experimental Validation

Mohammed Zerdani, Houcine Chafouk, Sid Ahmed El Mehdi Ardjoun

symmetry

MDPI

Article

Performance Analysis of a Dual-Inverter-Fed Open-End Winding Induction Machine under Asymmetrical Control: Theoretical Approach and Experimental Validation

Mohammed Zerdani [1,2], Houcine Chafouk [1,*] and Sid Ahmed El Mehdi Ardjoun [1,2,*]

[1] IRSEEM/ESIGELEC Laboratory, Normandy University of Rouen, 76000 Rouen, France; mohammed.zerdani@univ-sba.dz
[2] IRECOM Laboratory, Djillali Liabes University, Sidi Bel-Abbes 22000, Algeria
* Correspondence: houcine.chafouk@esigelec.fr (H.C.); elmehdi.ardjoun@univ-sba.dz (S.A.E.M.A.); Tel.: +33-32915821 (H.C.)

Abstract: Currently, power trains based on an Open-End Winding Induction Machine fed by a Dual Inverter (DI-OEWIM) are attracting a great deal of interest in various modern industrial applications. However, applying symmetrical control to this system (DI-OEWIM), which is symmetrical in nature, will lead to malfunction. Therefore, the objective of this paper is to explore the influence of asymmetric control on the performance of this system. The principle of this study is to create an asymmetrical control by integrating a phase-shift angle in the Space Vector Pulse Width Modulation (SVPWM) strategy. We then evaluate the impact of these angles on various performances, such as the Total Harmonic Distortion (THD), power losses, Common Mode Voltage (CMV), Zero-Sequence Voltage (ZSV), rotation speed and torque ripple of this system. This study was carried out in the Matlab/Simulink environment and was validated experimentally using the dSPACE 1104 board. The results show that the different angles have significant effects on the overall performance of this system.

Keywords: asymmetrical control; Dual Inverters; Open-End Winding; power losses; common mode voltage; THD; torque ripple; zero-sequence voltage

Citation: Zerdani, M.; Chafouk, H.; Ardjoun, S.A.E.M. Performance Analysis of a Dual-Inverter-Fed Open-End Winding Induction Machine under Asymmetrical Control: Theoretical Approach and Experimental Validation. *Symmetry* **2024**, *16*, 395. https://doi.org/10.3390/sym16040395

Academic Editor: Vasilis K. Oikonomou

Received: 28 January 2024
Revised: 26 February 2024
Accepted: 12 March 2024
Published: 28 March 2024

1. Introduction

In recent years, the ongoing development of power electronics converter technologies [1–4] has significantly shaped the electrical landscape. Among the notable advances, Dual-Inverter-fed Open-Winding Induction Machines (DI-OEWIMs) have attracted increasing interest in industrial electrical applications, as well as in modern electric traction systems, such as electric vehicles, trains, ships and aircraft [5–13].

Compared to conventional Induction Motor (IM) drives, DI-OEWIMs manage to generate equivalent torque with only half of the DC bus voltages [14,15]. In addition, DI-OEWIMs show a significant improvement in the waveform of voltages and currents, reducing their harmonic distortion (THD), and demonstrate a performance equivalent to that of IMs driven by three-level inverters [16–18]. Unlike conventional IM drives, the OEWIM drive offers a number of advantages, including a distributed drive configuration and an improved reliability through fault-tolerant operation [15], as well as the simplicity of decoupled control methods [19] and the absence of neutral point fluctuations [20].

However, this configuration is not without its drawbacks. These include overcharging (it damages capacitor) due to unequal DC bus voltages when using two isolated DC power supplies [19]. In addition, the direct interconnection of two inverters with a single DC bus leads to Zero-Sequence Voltage (ZSV) problems [21]. Moreover, high-frequency switching of inverter switches introduces the presence of a Common-Mode Voltage (CMV) [22–24].

The major problem of DI-OEWIM configuration is due to its symmetry. In this context, applying symmetrical control to such a system would make it impossible to operate [25–27]. In the literature, various studies have been carried out to overcome these problems and improve the performance of the DI-OEWIM, particularly with regard to Total Harmonic Distortion (THD), CMV, power losses, torque ripple and ZSV.

The authors in [28] presented an asymmetric nested inverter strategy, aimed at eliminating the ZSV through Pulse-Width Modulation (PWM) averaged sampling, based on the strategic placement of the zero-vector period. However, the impact of this strategy on THD, torque ripple and CMV behavior has not been addressed. In an anterior publication [21], an asymmetric near-state PWM strategy was introduced to improve THD, but without consideration of the issues related to power losses, torque ripple and CMV. Another contribution [29] developed an asymmetric strategy based on the selection of optimal vectors, although there was no in-depth study of CMV behavior or the issue of overcharging. In [24], a strategy based on the use of a dual-vector PWM method was put forward, however it did not include an analysis of the CMV behavior. The authors of [30] presented different asymmetric approaches to the PWM strategy, but neglected torque ripples. An improved asymmetric Zero-Sequence Current (ZSC) hysteresis control strategy was proposed in [31], but without any analysis of the CMV behavior, torque ripples and power losses. In [32], an asymmetric PWM strategy with a 120° phase shift between the two inverters was suggested, although the impact on power losses and torque ripples was not studied. In [6], the authors introduced a new asymmetric strategy called modified SVPWM, but this was done without any analysis of the torque ripples for phase-shift angles of 90° and 120°. The contributors to [26] applied an asymmetric PWM strategy with different phase-shift angle values, yet they did not evaluate the impact on power losses and torque ripples. In contrast, the contribution of [27] focused on the application of asymmetric discontinuous PWM strategies with a phase-shift angle of 120° and power loss optimization, although the THD was degraded and the effect on torque ripple was not investigated.

Previous works have focused on the application of asymmetrical control strategies, albeit with a unique phase-shift angle. However, such works have not exhaustively addressed all performance criteria, such as attenuation of THD, CMV, ZSV, power losses, torque ripple and overcharging.

The main objective of this paper is to improve the understanding of asymmetrical control in DI-OEWIM. The specific objectives are to study the impact of different phase-shift angles (60°, 120°, 180°, 240°, 300° and 360°) on performance parameters, including THD, CMV, ZSV, power losses and torque ripples.

The novelty of this study lies in its in-depth evaluation of asymmetrical control strategies over a range of phase-shift angles, thus providing insights for optimizing DI-OEWIM performance in terms of THD reduction, CMV suppression, ZSV mitigation, power loss minimization and torque ripple mitigation. In addition, this study uses both numerical simulations and experimental validations to ensure a better analysis.

To achieve these contributions, the remainder of the paper is structured as follows: Section 2 provides a visualization of the problems associated with the DI-OEWIM system. Section 3 presents the asymmetric technique suggested to control this system. Simulation results are analyzed in Section 4, followed by a review of experimental results in Section 5. Finally, Section 6 presents the conclusions drawn from the proposed study, as well as future perspectives.

2. Position of the Problem

Figure 1 shows the configuration of the DI powered by a common DC bus. We opted for this power supply structure in order to avoid overcharging problems. Indeed, overcharging can cause damage to the capacitor and generate undesirable harmonics in the

motor phase voltage [33]. In this structure, the voltage applied to the OEWIM terminal is expressed by the following relationship [27]:

$$V_{DI} = V_{inv,1} - V_{inv,2} \tag{1}$$

where $V_{inv,1}$ and $V_{inv,2}$ represent the reference voltages of the first and second inverters, respectively. The voltage generated by each inverter can be expressed by Equation (2), and the vector representation of the two inverters is shown in Figure 2.

$$V_{inv,x} = \sqrt{\frac{2}{3}} V_{dc} \left(S_{d1} + \gamma\, S_{d3} + \gamma^2\, S_{d5} \right) \; where \; \gamma = e^{j\frac{2\pi}{3}} \tag{2}$$

where $x(= 1 \text{ and } 2)$ represents the inverter number, V_{dc} represents the DC bus voltage and S_{d1}, S_{d3} andS_{d5} represent the switching states of the two inverters or $d(= i \text{ and } j)$.

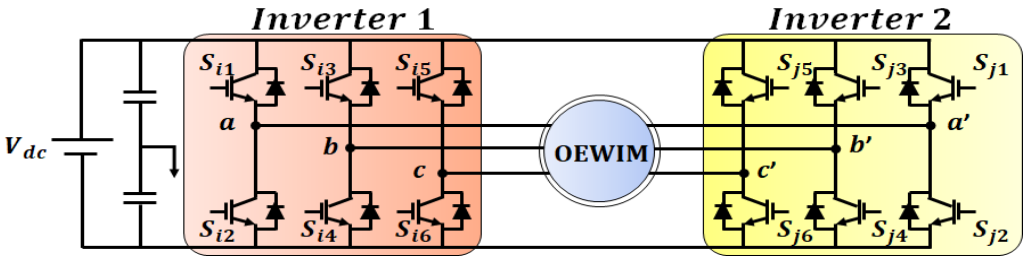

Figure 1. DI-OEIWM structure fed by a common DC bus.

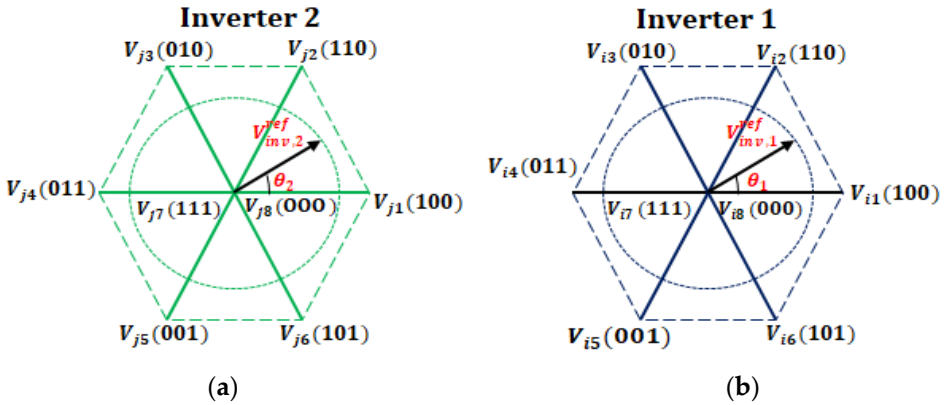

Figure 2. Voltage space vector representation of: (**a**) inverter 1, (**b**) inverter 2.

Figure 2 shows the voltage vectors applied to each inverter in the DI system. The DI operating principle relies on combining the voltage vectors of the two inverters to generate the rotating magnetic field required for motor operation. However, in this symmetrical structure, if the same voltage vectors are applied to both inverters (as illustrated in Figure 2), this leads to a cancellation of the magnetic fields and, thus, to the stoppage of induction motor operation. To remedy this situation, it is essential to apply asymmetrical control strategies. These strategies are based on creating a phase shift between the voltage vectors of the two inverters. This approach makes it possible to generate a total of 64 $\left(2^3 \times 2^3\right)$ possible states.

The spatial representation of the vectors produced by the DI is shown in Figure 3, which is similar to that of a three-level inverter.

However, this configuration has disadvantages, such as (i) the presence of the CMV component, which is generated due to high-frequency switching [22], (ii) the presence of the ZSV component, which is due to the common connection of both inverters to the DC bus [21] and (iii) degradation of system efficiency, which is due to an increase in the number of switches in the system compared to conventional configurations [27].

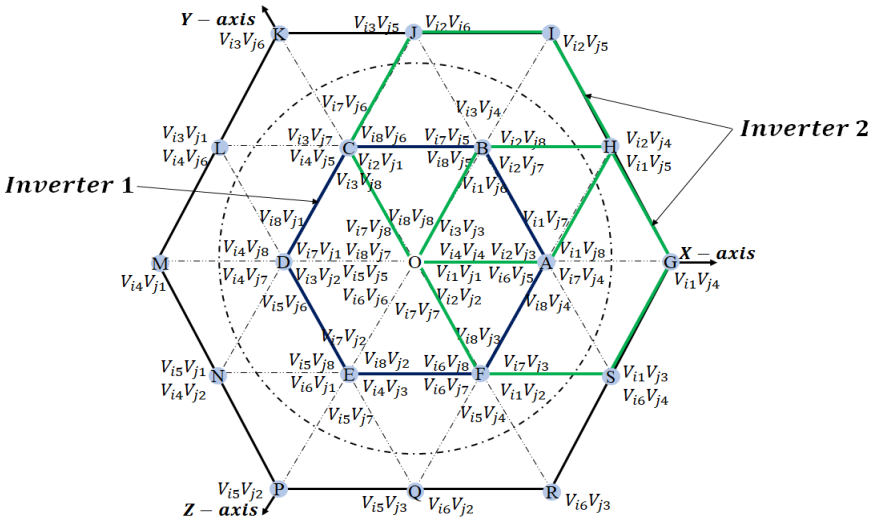

Figure 3. Representation of DI voltage vectors supplied by a common DC bus.

Equations (3)–(5) are used to express the CMV for each inverter and for the DI. The combination of different DI vectors generates distinct levels of CMV. Table 1 shows the various CMV levels and their associated vectors.

$$V_{cmv_{inv,1}} = \frac{S_{i1} + S_{i3} + S_{i5}}{3} V_{dc} \tag{3}$$

$$V_{cmv_{inv,2}} = \frac{S_{j1} + S_{j3} + S_{j5}}{3} V_{dc} \tag{4}$$

$$V_{cmv_{DI}} = \frac{V_{cmv_{inv,1}} + V_{cmv_{inv,2}}}{2} = \frac{(S_{i1} + S_{i3} + S_{i5}) + (S_{j1} + S_{j3} + S_{j5})}{6} V_{dc} \tag{5}$$

Table 1. CMV levels and their associated vectors.

CMV Level	Associated Vectors
$-V_{dc}/2$	$V_{i8}V_{j8}$
$-V_{dc}/3$	$V_{i1}V_{j8}$, $V_{i3}V_{j8}$, $V_{i5}V_{j8}$, $V_{i8}V_{j1}$, $V_{i8}V_{j3}$, $V_{i8}V_{j5}$
$-V_{dc}/6$	$V_{i1}V_{j1}$, $V_{i1}V_{j3}$, $V_{i1}V_{j5}$, $V_{i3}V_{j1}$, $V_{i3}V_{j3}$, $V_{i3}V_{j5}$, $V_{i5}V_{j1}$, $V_{i5}V_{j3}$, $V_{i5}V_{j5}$, $V_{i2}V_{j8}$, $V_{i4}V_{j8}$, $V_{i6}V_{j8}$, $V_{i8}V_{j2}$, $V_{i8}V_{j4}$, $V_{i8}V_{j6}$
0	$V_{i8}V_{j7}$, $V_{i1}V_{j2}$, $V_{i1}V_{j4}$, $V_{i1}V_{j6}$, $V_{i3}V_{j2}$, $V_{i3}V_{j4}$, $V_{i3}V_{j6}$, $V_{i5}V_{j2}$, $V_{i5}V_{j4}$, $V_{i5}V_{j6}$, $V_{i2}V_{j1}$, $V_{i2}V_{j3}$, $V_{i2}V_{j5}$, $V_{i4}V_{j1}$, $V_{i4}V_{j3}$, $V_{i4}V_{j5}$, $V_{i6}V_{j1}$, $V_{i6}V_{j3}$, $V_{i5}V_{j5}$, $V_{i7}V_{j8}$
$V_{dc}/6$	$V_{i2}V_{j2}$, $V_{i2}V_{j4}$, $V_{i2}V_{j6}$, $V_{i4}V_{j2}$, $V_{i4}V_{j4}$, $V_{i4}V_{j6}$, $V_{i6}V_{j2}$, $V_{i6}V_{j4}$, $V_{i6}V_{j6}$, $V_{i1}V_{j7}$, $V_{i3}V_{j7}$, $V_{i5}V_{j7}$, $V_{i7}V_{j1}$, $V_{i7}V_{j3}$, $V_{i7}V_{j5}$
$V_{dc}/3$	$V_{i2}V_{j7}$, $V_{i4}V_{j7}$, $V_{i6}V_{j7}$, $V_{i7}V_{j2}$, $V_{i7}V_{j4}$, $V_{i7}V_{j6}$
$V_{dc}/2$	$V_{i7}V_{j7}$

The calculation of this ZSV is based on the CMV of both inverters and can be expressed by Equations (6) and (7) [27]. This ZSV is generated by combining the various voltage vectors, as shown in Table 2.

$$V_{zsv_{DI}} = V_{cmv_{inv,1}} - V_{cmv_{inv,2}} \tag{6}$$

$$V_{zsv_{DI}} = \frac{(S_{i1} - S_{j1}) + (S_{i3} - S_{j3}) + (S_{i5} - S_{j5})}{3} V_{dc} \tag{7}$$

Table 2. ZSV levels and their associated vectors.

ZSV Level	Associated Vectors
$-V_{dc}$	$V_{i8}V_{j7}$
$-2V_{dc}/3$	$V_{i8}V_{j4}$, $V_{i8}V_{j6}$, $V_{i8}V_{j2}$, $V_{i5}V_{j7}$, $V_{i3}V_{j7}$, $V_{i1}V_{j7}$
$-V_{dc}/3$	$V_{i8}V_{j5}$, $V_{i8}V_{j3}$, $V_{i5}V_{j4}$, $V_{i3}V_{j4}$, $V_{i8}V_{j1}$, $V_{i5}V_{j2}$, $V_{i3}V_{j6}$, $V_{i3}V_{j2}$, $V_{i4}V_{j7}$, $V_{i1}V_{j4}$, $V_{i1}V_{j6}$, $V_{i1}V_{j2}$, $V_{i6}V_{j7}$, $V_{i2}V_{j7}$, $V_{i5}V_{j6}$
0	$V_{i1}V_{j3}$, $V_{i6}V_{j4}$, $V_{i2}V_{j4}$, $V_{i1}V_{j5}$, $V_{i3}V_{j5}$, $V_{i2}V_{j6}$, $V_{i4}V_{j6}$, $V_{i3}V_{j1}$, $V_{i5}V_{j1}$, $V_{i4}V_{j2}$, $V_{i5}V_{j3}$, $V_{i6}V_{j2}$, $V_{i7}V_{j7}$, $V_{i8}V_{j8}$, $V_{i1}V_{j1}$, $V_{i5}V_{j5}$, $V_{i4}V_{j4}$, $V_{i3}V_{j3}$, $V_{i2}V_{j2}$, $V_{i1}V_{j1}$
$V_{dc}/3$	$V_{i5}V_{j8}$, $V_{i3}V_{j8}$, $V_{i4}V_{j5}$, $V_{i4}V_{j3}$, $V_{i1}V_{j8}$, $V_{i2}V_{j5}$, $V_{i6}V_{j3}$, $V_{i2}V_{j3}$, $V_{i7}V_{j4}$, $V_{i4}V_{j1}$, $V_{i6}V_{j1}$, $V_{i2}V_{j1}$, $V_{i7}V_{j6}$, $V_{i7}V_{j2}$, $V_{i6}V_{j5}$
$2V_{dc}/3$	$V_{i4}V_{j8}$, $V_{i6}V_{j8}$, $V_{i2}V_{j8}$, $V_{i7}V_{j5}$, $V_{i7}V_{j3}$, $V_{i7}V_{j1}$
V_{dc}	$V_{i7}V_{j8}$

Power electronics literature identifies two types of losses in inverters: (i) switching losses (P_{sw}) and (ii) conduction losses of the interrupter $\left(P_{cond,Sij}\right)$, with the conduction losses of the bottom diode ($P_{cond,BD}$). These losses can be calculated using the following formulas [27]:

$$P_{sw} = \left[\frac{1}{2}v_{sw}(t)\times i_{sw}(t) \times \left(t_{sw,on} + t_{sw,off}\right)\right] \times f_{sw} \tag{8}$$

$$P_{con,Sij} = \frac{V_{on,Sij} \times i_{sw}(t) \times t_{on}}{T_{sw}} \tag{9}$$

$$P_{con,BD} = \frac{V_{on,Sij}\times i_{sw}(t) \times t_{off}}{T_{sw}} \tag{10}$$

The variable v_{sw} represents the voltage imposed by the switch in the off state. The term v_{on} designates the voltage dissipated in the on state, while i_{sw}, equal to i_{on}, designates the current flowing through the switch in the on state. f_{sw} represents the switching frequency and T_{sw} is defined as the switching period.

3. Proposed Solutions

The association of inverter to machine has a significant impact on power quality and efficiency. In order to optimize the performance resulting from the association of the DI with the OEWIM, it is vital to implement a sophisticated asymmetrical control technique. Among these techniques, SVPWM is widely recognized and used in the industrial sector. To study the effect of asymmetrical SVPWM, this section first presents the principle of the conventional SVPWM strategy, then explores the principle of asymmetrical SVPWM (ASVPWM).

3.1. Conventional SVPWM Principle

The conventional SVPWM strategy is a modulation technique based on mathematical transformations, using the Clarke transform (see Equation (11)). To determine the duration of the active vectors to be applied [34], the modulation period is completed by using the zero vectors (V_7 and V_8). Figure 4 shows a representation of the vectors corresponding to all possible inverter states, forming the vertices of a hexagon on the $\alpha\beta$ plan.

$$\begin{bmatrix} V_\alpha \\ V_\beta \end{bmatrix} = \sqrt{\frac{2}{3}} \begin{bmatrix} 1 & -\frac{1}{2} & -\frac{1}{2} \\ 0 & \frac{\sqrt{3}}{2} & -\frac{\sqrt{3}}{2} \end{bmatrix} \begin{bmatrix} V_a \\ V_b \\ V_c \end{bmatrix} \tag{11}$$

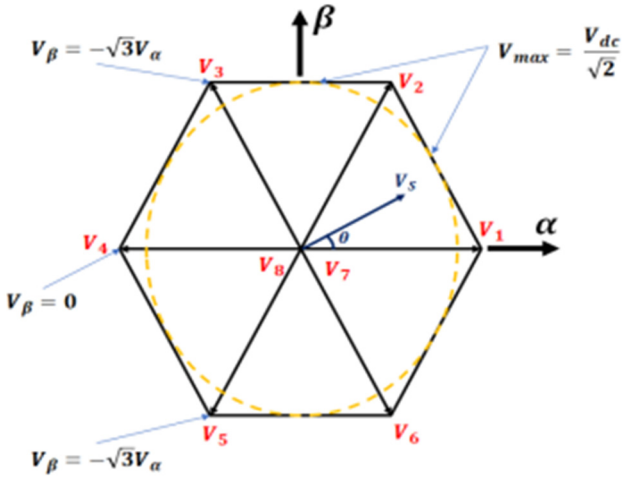

Figure 4. Representation of DI voltage vectors supplied by a common DC bus.

Looking at Equation (11) and Figure 4, the projections in the $\alpha\beta$ plan can be derived. These projections can influence the V_s vector, especially when applying various voltage vectors, as demonstrated in Table 3.

Table 3. Inverter voltage vectors for SVPWM control.

Vector	S_1	S_3	S_5	V_α	V_β	V_s
V_1	1	0	0	$\frac{2V_{dc}}{\sqrt{6}}$	0	$\frac{2}{3}V_{dc}$
V_2	1	1	0	$\frac{V_{dc}}{\sqrt{6}}$	$\frac{V_{dc}}{\sqrt{2}}$	$\frac{2}{3}V_{dc}e^{j\frac{\pi}{3}}$
V_3	0	1	0	$-\frac{V_{dc}}{\sqrt{6}}$	$\frac{V_{dc}}{\sqrt{2}}$	$\frac{2}{3}V_{dc}e^{j\frac{2\pi}{3}}$
V_4	0	1	1	$-\frac{2V_{dc}}{\sqrt{6}}$	0	$\frac{2}{3}V_{dc}e^{j\pi}$
V_5	0	0	1	$-\frac{V_{dc}}{\sqrt{6}}$	$-\frac{V_{dc}}{\sqrt{2}}$	$\frac{2}{3}V_{dc}e^{j\frac{4\pi}{3}}$
V_6	1	0	1	$\frac{V_{dc}}{\sqrt{6}}$	$-\frac{V_{dc}}{\sqrt{2}}$	$\frac{2}{3}V_{dc}e^{j\frac{5\pi}{3}}$
V_7	1	1	1	0	0	0
V_8	0	0	0	0	0	0

The rotating reference vector V_s and the angle θ can be calculated using the following formulae:

$$V_s = \sqrt{V_\alpha^2 + V_\beta^2} \tag{12}$$

$$\theta = atan\left(\frac{V_\beta}{V_\alpha}\right) \tag{13}$$

The durations of the SVPWM conductions are calculated according to the following formulas:

$$T_k = \frac{V_{s,ref}}{V_k}\left(cos\theta_k - \frac{sin\theta_k}{\sqrt{3}}\right) \tag{14}$$

$$T_{k+1} = \frac{V_{s,ref}}{V_{k+1}}\left(cos\theta_{k+1} - \frac{sin\theta_{k+1}}{\sqrt{3}}\right) \tag{15}$$

$$T_0 = T_{sw} - (T_k + T_{k+1}) \tag{16}$$

Knowing that for a sector k, $\theta_{k+1} = \theta_k - (k-1)\frac{\pi}{3}$, where $k = 1, 2, \ldots, 6$.
The entire SVPWM process is illustrated in Figure 5.

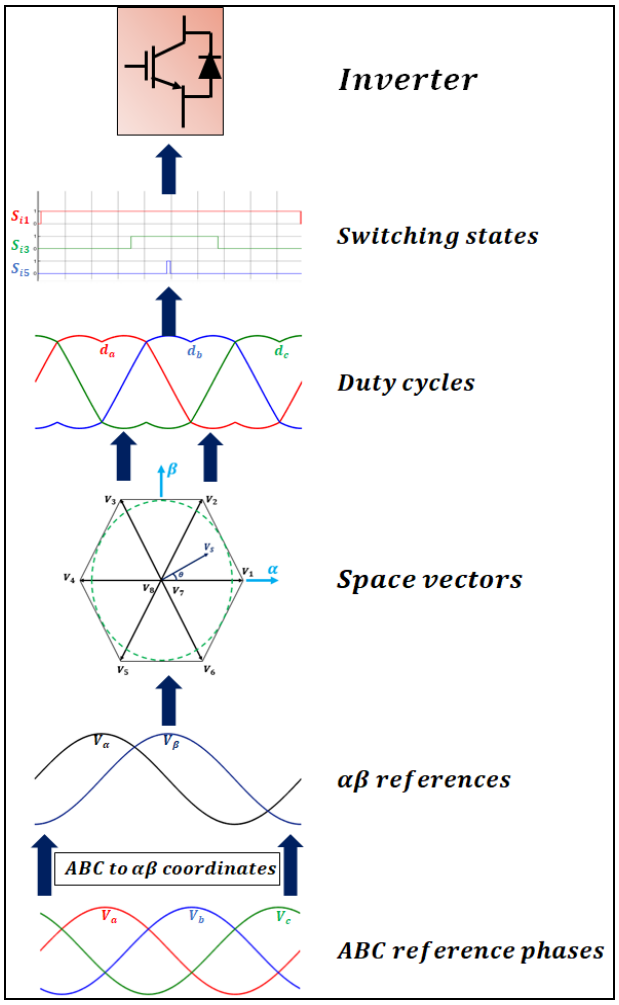

Figure 5. SVPWM strategy process.

3.2. Asymmetrical SVPWM

As mentioned earlier in Section 2, if both ends of the motor receive the same voltage with the same phase shift (symmetrical control), the motor will not rotate. To rotate the OEWIM, an asymmetrical control technique must be applied, where a phase-shift angle θ_{DI} ($\theta_{DI} = \theta_{inv,1} - \theta_{inv,2}$) must be introduced into the voltages generated by one of the inverters. So, asymmetrical control of a DI system relies on creating a phase shift between the main inverter and the auxiliary inverter, or vice versa.

Consequently, the reference voltages of the main and auxiliary inverters can be expressed as follows:

$$\begin{cases} v_{inv,1_a}^{ref} = Vsin(\omega t) \\ v_{inv,1_b}^{ref} = Vsin\left(\omega t - \frac{2\pi}{3}\right) \\ v_{inv,1_c}^{ref} = Vsin\left(\omega t + \frac{2\pi}{3}\right) \end{cases} \quad (17)$$

$$\begin{cases} v_{inv,2_{a'}}^{ref} = Vsin(\omega t + \theta_{DI}) \\ v_{inv,2_{b'}}^{ref} = Vsin\left(\omega t - \frac{2\pi}{3} + \theta_{DI}\right) \\ v_{inv,2_{c'}}^{ref} = Vsin\left(\omega t + \frac{2\pi}{3} + \theta_{DI}\right) \end{cases} \quad (18)$$

According to Equations (17) and (18), the control signals of the second inverter are adjusted (with angle θ_{DI}) relative to the first inverter within the same sampling period.

Figure 6 shows the DI switching states and their voltages for the two distinct strategies (symmetrical and asymmetrical). When applying symmetrical control, it should be noted

that the same voltage vectors are applied to the OEWIM by both inverters, resulting in identical voltages ($V_{inv,1} = V_{inv,2}$). Since the voltage applied to the OEWIM is the subtraction between the two inverter voltages, this leads to a zero voltage for the DI ($V_{ij} = 0$). Consequently, the OEWIM will not operate, as shown in Figure 6a. On the other hand, when applying an asymmetrical control strategy (creating a phase-shift angle θ_{DI} between the reference voltages), the switching states of the second inverter are shifted compared to the switching states of the first inverter by the angle θ_{DI}. In this case, it should be noted that different voltage vectors will be applied to the OEWIM, generating two different voltages for the two inverters ($V_{inv,1} \neq V_{inv,2}$). This creates a voltage for the DI, inducing rotation of the OEWIM, as illustrated in Figure 6b.

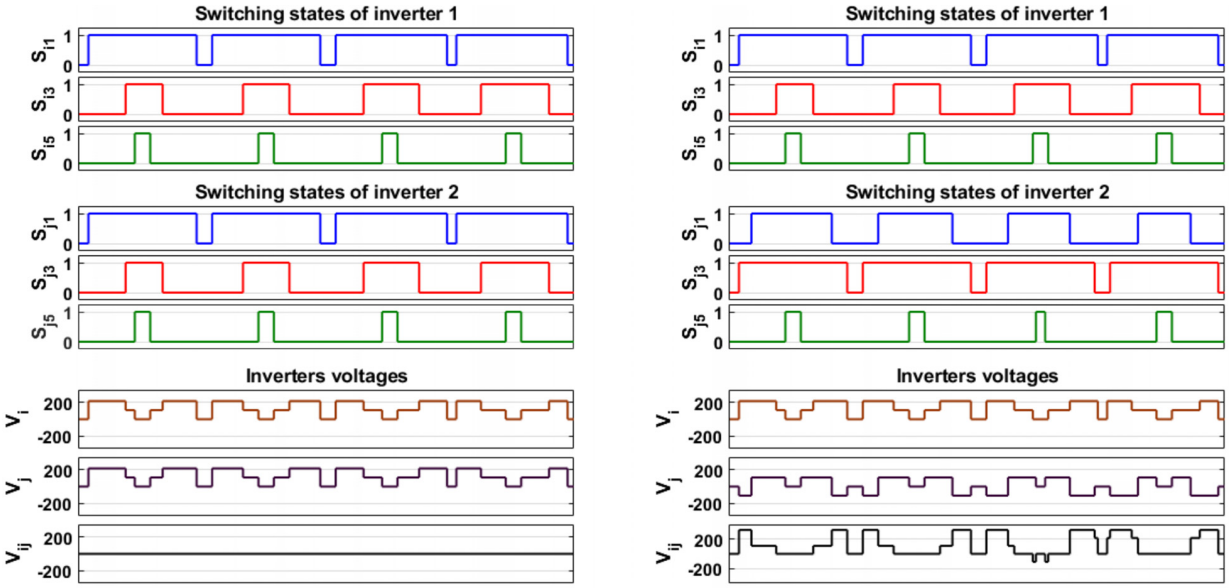

Figure 6. Control principle: (**a**) symmetrical, (**b**) asymmetrical.

However, the choice of this phase-shift angle θ_{DI} generates different combinations of switching vectors (as illustrated in Figure 3), and this has an impact on DI-OEWIM performances, particularly with regard to CMV and ZSV phenomena. Table 4 lists several ASVPWM control strategies, and each strategy is associated with a specific value of angle θ_{DI}, as well as their impacts on CMV and ZSV. In this article, the values of θ_{DI} have been chosen according to the tension vectors generated by the hexagon decomposition, in line with the principle of the SVPWM strategy.

Table 4. Associated vectors for each angle θ_{DI} and their effects on CMV and ZSV.

Strategy	θ_{DI}	Associated Vectors	CMV Levels	ZSV Levels
ASVPWM1	60°	$V_{i8}V_{j8}$; $V_{i7}V_{j7}$; $V_{i1}V_{j2}$; $V_{i2}V_{j3}$; $V_{i3}V_{j4}$; $V_{i4}V_{j5}$; $V_{i5}V_{j6}$; $V_{i6}V_{j1}$	$(-V_{dc}/2; -V_{dc}/6;$ $0; V_{dc}/6; V_{dc}/2)$	$(-V_{dc}/3; 0;$ $V_{dc}/3)$
ASVPWM2	120°	$V_{i8}V_{j8}$; $V_{i7}V_{j7}$; $V_{i1}V_{j3}$; $V_{i2}V_{j4}$; $V_{i3}V_{j5}$; $V_{i4}V_{j6}$; $V_{i5}V_{j1}$; $V_{i6}V_{j2}$	$(-V_{dc}/2; -V_{dc}/6;$ $V_{dc}/6; V_{dc}/2)$	0
ASVPWM3	180°	$V_{i8}V_{j8}$; $V_{i7}V_{j7}$; $V_{i1}V_{j4}$; $V_{i2}V_{j5}$; $V_{i3}V_{j6}$; $V_{i4}V_{j1}$; $V_{i5}V_{j2}$; $V_{i6}V_{j3}$	$(-V_{dc}/2; -V_{dc}/6;$ $0; V_{dc}/6; V_{dc}/2)$	$(-V_{dc}/3; 0;$ $V_{dc}/3)$
ASVPWM4	240°	$V_{i8}V_{j8}$; $V_{i7}V_{j7}$; $V_{i1}V_{j5}$; $V_{i2}V_{j6}$; $V_{i3}V_{j1}$; $V_{i4}V_{j2}$; $V_{i5}V_{j3}$; $V_{i6}V_{j4}$	$(-V_{dc}/2; -V_{dc}/6;$ $V_{dc}/6; V_{dc}/2)$	0
ASVPWM5	300°	$V_{i8}V_{j8}$; $V_{i7}V_{j7}$; $V_{i1}V_{j6}$; $V_{i2}V_{j1}$; $V_{i3}V_{j2}$; $V_{i4}V_{j3}$; $V_{i5}V_{j4}$; $V_{i6}V_{j5}$	$(-V_{dc}/2; -V_{dc}/6;$ $0; V_{dc}/6; V_{dc}/2)$	$(-V_{dc}/3; 0;$ $V_{dc}/3)$
ASVPWM6	360°	$V_{i8}V_{j8}$; $V_{i7}V_{j7}$; $V_{i1}V_{j1}$; $V_{i2}V_{j2}$; $V_{i3}V_{j3}$; $V_{i4}V_{j4}$; $V_{i5}V_{j5}$; $V_{i6}V_{j6}$	$(-V_{dc}/2; -V_{dc}/6;$ $V_{dc}/6; V_{dc}/2)$	0

4. Simulation Results

To assess the influence of the ASVPWM techniques presented in Table 4 on the performances (THD, losses, CMV, ZSV and torque ripples) of an OEWIM drive system, a series of tests was carried out using the MATLAB/Simulink environment. The simulation model is shown in Figure A1 (Appendix A). The simulation was run for the OEWIM, whose characteristics are presented in Table A1 (Appendix B).

In this test, we simulated the application of various ASVPWM techniques outlined in Table 4. Reference voltages were generated at a reference speed of 150 rad/s, with the control signals being produced at a switching frequency of 2 kHz. Additionally, a load of 7 N.m was applied. For the calculation of switching losses in the different techniques, the following were taken into account:

- The characteristics of the switch module (IGBT-SKM150GB123D) were used to calculate losses.
- The switching time parameters, $t_{sw,on}$ equivalent to 1.5 µs and $t_{\mathrm{sw,off}}$ equivalent to 3 µs [27].
- To ensure sufficient accuracy in calculating losses, the simulation step size was set at 1 µs.

Figure 7 shows the responses of the voltages generated by the DI, the OEWIM stator currents, the THDs and the electromagnetic torque for each of the ASVPWM1, ASVPWM2, ASVPWM3, ASVPWM4 and ASVPWM5 strategies. Figure 8 explains the switching states of each inverter and their respective impacts on CMV and ZSV when using each ASVPWM strategy. Furthermore, Figure 9 details the switching losses of the top switch, the conduction losses of the top switch and the conduction losses of the bottom diode. Finally, a concise summary of the results of this test is presented in Table 5.

The results obtained from this test lead to the following observations:

- THDs
  - The ASVPWM2 strategy significantly improves voltage THD, reaching a value of 81.88%.
  - On the other hand, the ASVPWM4 strategy stands out for its improved current THD, with a value of 23.17%.
- Torque T_e ripples
  - ASVPWM1 and ASVPWM5 techniques are effective in reducing electromagnetic torque ripples, with values between 5 N.m and 9 N.m.
- CMV and ZSV
  - The ASVPWM1, ASVPWM3 and ASVPWM5 strategies generate five-level CMVs $\left(-\frac{V_{dc}}{2}; -\frac{V_{dc}}{6}; 0; \frac{V_{dc}}{6}; \frac{V_{dc}}{2}\right)$ equivalent to $\pm\frac{V_{dc}}{2} = \pm 163\text{V}$, $\pm\frac{V_{dc}}{6} = \pm 54.33\text{V}$ and 0. In addition, they have three-level ZSVs $\left(-\frac{V_{dc}}{3}; 0; \frac{V_{dc}}{3}\right)$, which are $\pm\frac{V_{dc}}{3} = \pm 108.66\text{V}$ and 0.
  - In contrast, the ASVPWM2 and ASVPWM4 strategies generate four-level CMVs $\left(-\frac{V_{dc}}{2}; -\frac{V_{dc}}{6}; \frac{V_{dc}}{6}; \frac{V_{dc}}{2}\right)$, which are $\pm\frac{V_{dc}}{2} = \pm 163\text{V}$ and $\pm\frac{V_{dc}}{6} = \pm 54.33\text{V}$. However, they eliminate ZSV completely due to the phase-shift angles $\theta_{DI} = 120^\circ$ and $\theta_{DI} = 240^\circ$.
- Total DI losses
  - The ASVPWM2 and ASVPWM4 strategies stand out for their ability to minimize total losses in the DI, achieving a percentage of 6.66%. In comparison, ASVPWM1 and ASVPWM5 show less advantageous results.
  - On the other hand, compared with ASVPWM3, the application of ASVPWM1 and ASVPWM5 reduces total losses by 10.25%.

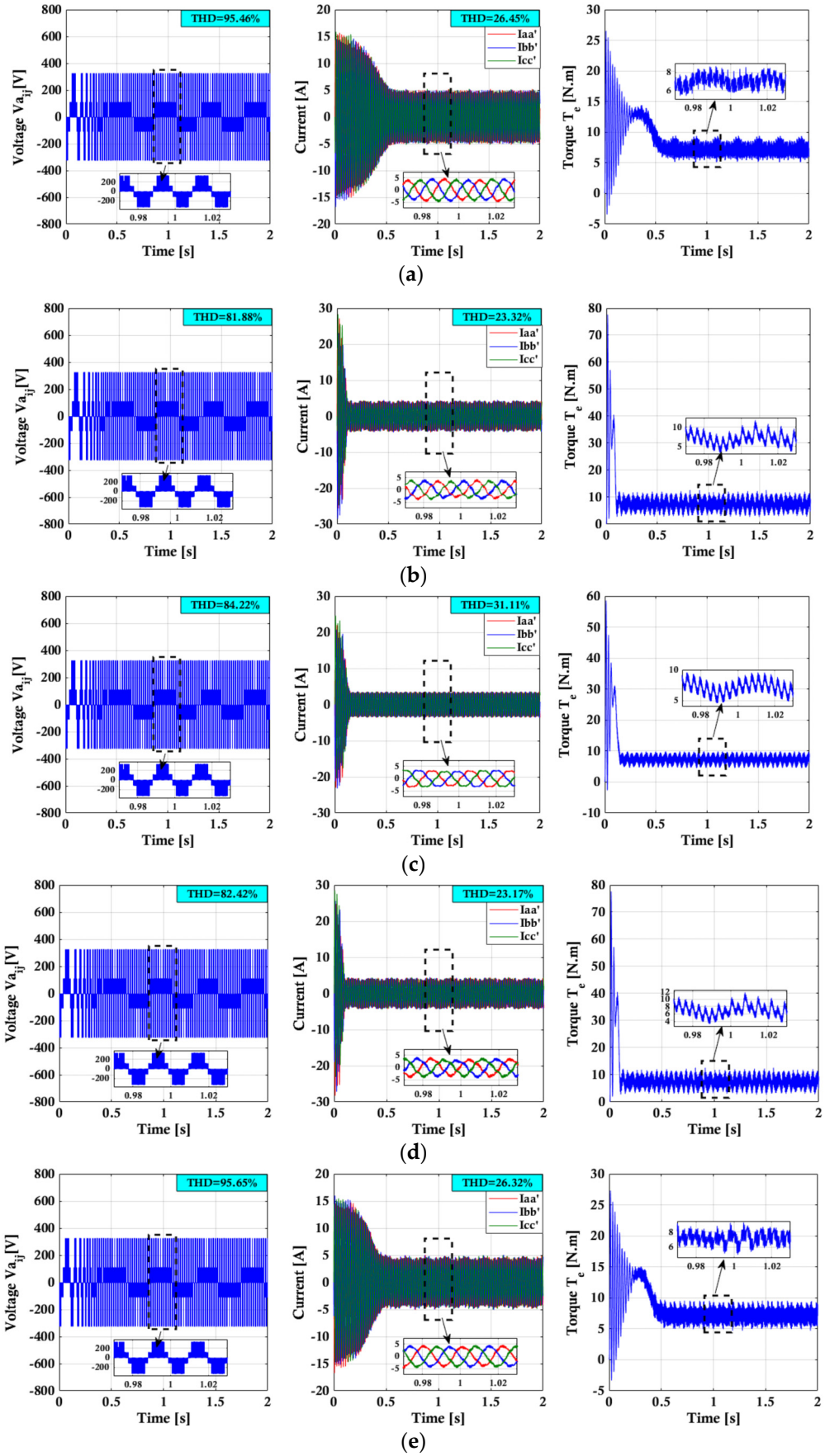

Figure 7. Voltage, current and electromechanical torque responses of the strategies: (**a**) ASVPWM1, (**b**) ASVPWM2, (**c**) ASVPWM3, (**d**) ASVPWM4, (**e**) ASVPWM5.

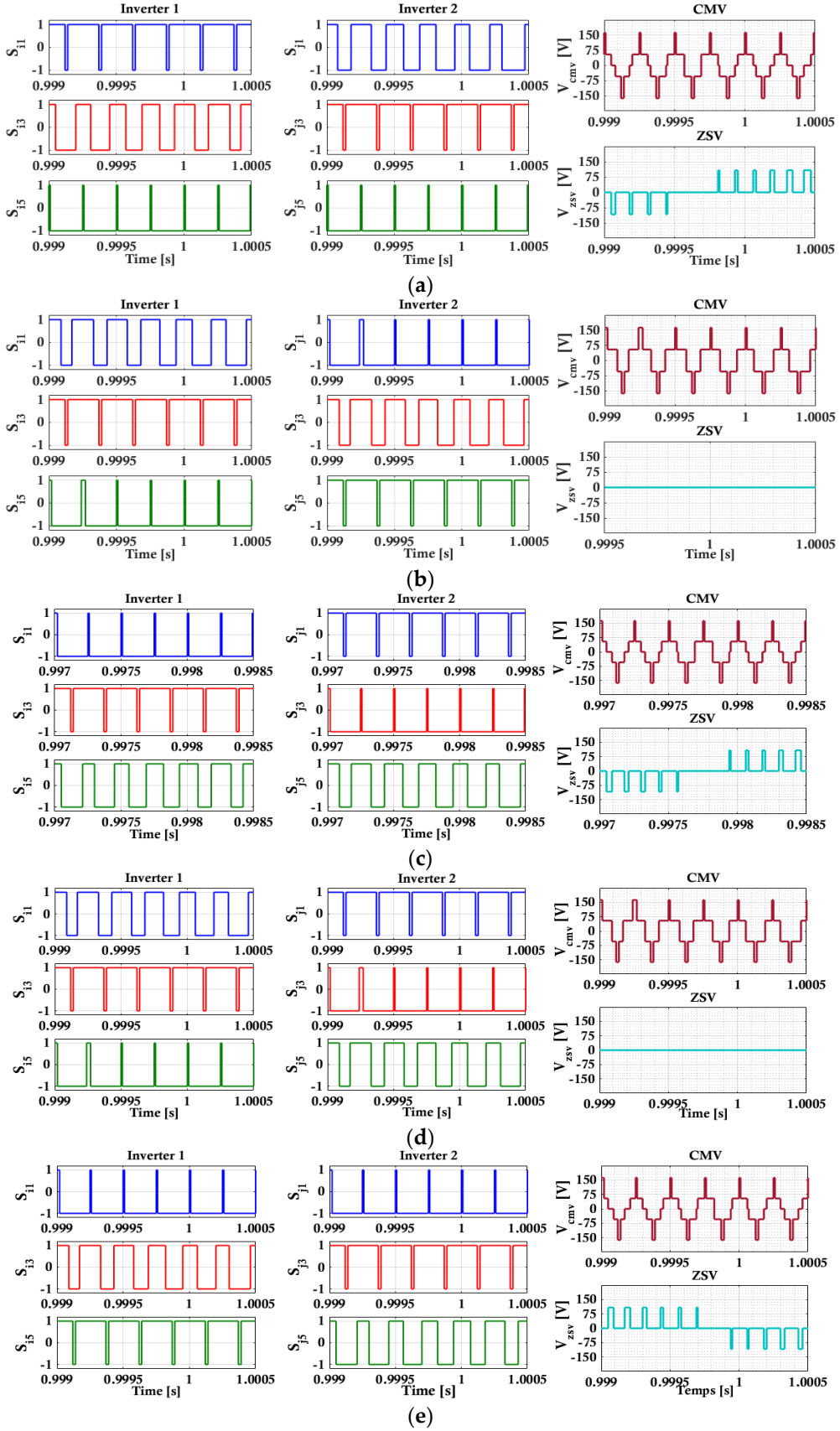

Figure 8. Switching states of the two inverters, the CMV and ZSV responses of the strategies: (**a**) ASVPWM1, (**b**) ASVPWM2, (**c**) ASVPWM3, (**d**) ASVPWM4, (**e**) ASVPWM5.

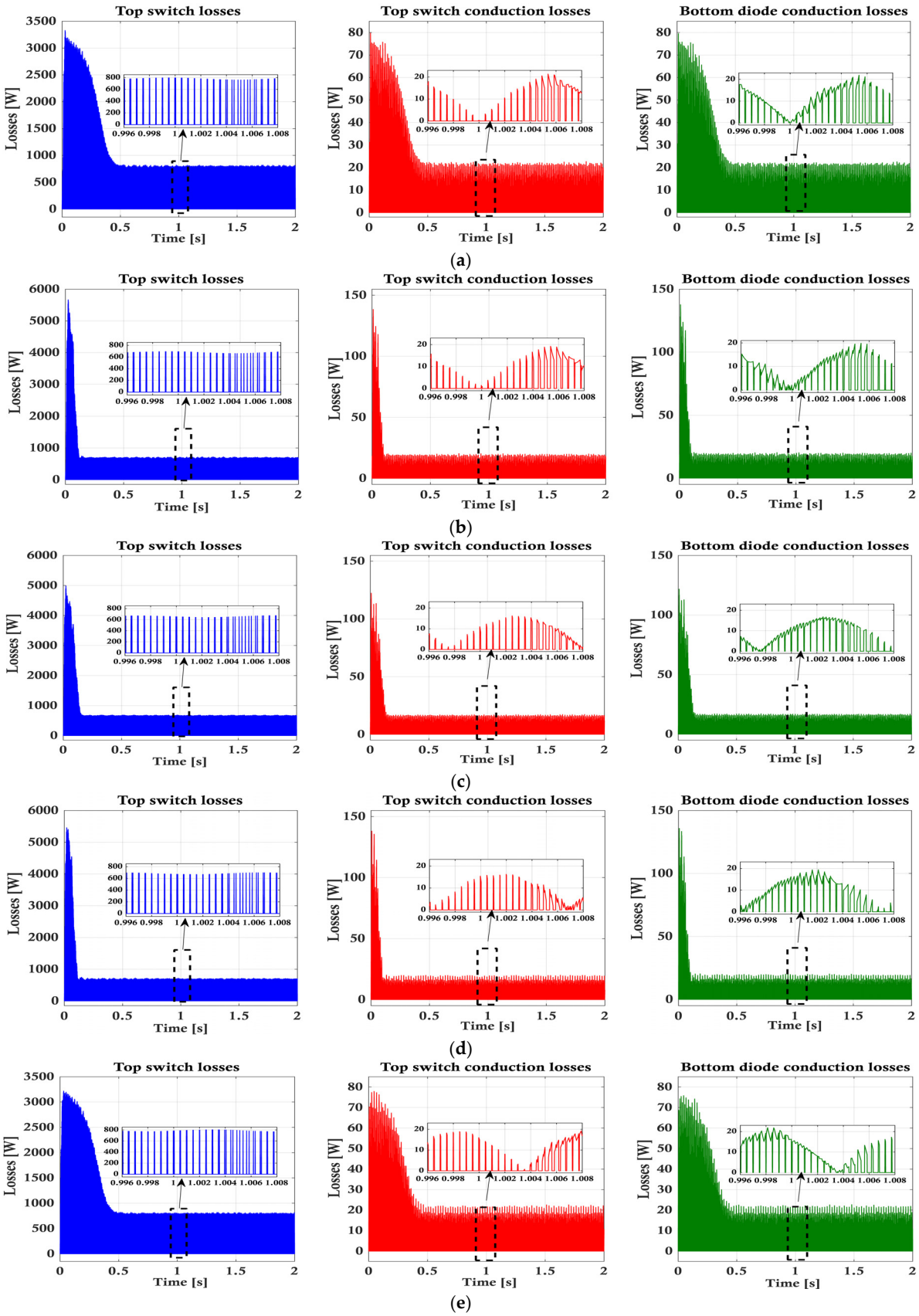

Figure 9. Switching losses and lower diode conductance losses for the strategies: (**a**) ASVPWM1, (**b**) ASVPWM2, (**c**) ASVPWM3, (**d**) ASVPWM4, (**e**) ASVPWM5.

Table 5. Summary of simulation results.

Strategy	THD		Total Losses of DI [W]	Highest Level of CMV [V]	Highest Level of ZSV [V]	Torque Ripple T_e [N.m]
	V [%]	I [%]				
ASVPWM1	95.46	26.43	750	$\pm\frac{326}{2}$	$\pm\frac{326}{3}$	[5; 11]
ASVPWM2	81.88	23.32	700	$\pm\frac{326}{2}$	0	[3.5; 12]
ASVPWM3	84.22	31.11	780	$\pm\frac{326}{2}$	$\pm\frac{326}{3}$	[2.5; 14]
ASVPWM4	82.42	23.17	700	$\pm\frac{326}{2}$	0	[3.5; 12]
ASVPWM5	95.65	26.32	750	$\pm\frac{326}{2}$	$\pm\frac{326}{3}$	[5; 10]
ASVPWM6	No defined	No defined	No defined	$\pm\frac{326}{2}$	0	No defined

The results obtained in this test, in terms of CMV and ZSV, confirm the consistency of these data with the previous results presented in Table 4. In addition, it can be noted that:

- The ASVPWM1 and ASVPWM5 strategies improve electromagnetic torque ripple.
- The ASVPWM2 and ASVPWM4 strategies prove more effective at improving voltage and current THD, as well as reducing total DI losses, respectively, while effectively eliminating ZSV.

5. Experimental Results

To evaluate the performance of ASVPWM techniques in real time, an experimental set-up was developed, as shown in Figure 10. System parameters are detailed in Table A1 in Appendix B. The device consists of a 1.5 kW DI-driven OEWIM, powered by a common DC bus of 326 V, and the system operates without filtering. This OEWIM drives a DC machine acting as a mechanical load. SVPWM control techniques have been implemented on a dSPACE 1104 board, with programming carried out using MATLAB/Simulink (see Figure A2, Appendix A) with reference to the block diagram shown in Figure 11. The experiment aimed to reproduce the test already carried out by the simulation, as presented in Section 4. This test was carried out with a switching frequency of 2 kHz and a sampling frequency of 10 kHz, along with a load of 7 N.m. Performance analysis was carried out using an oscilloscope to visualize switching states, torque, currents, CMV and ZSV. In addition, a spectrum analyzer was used to measure THD, as well as DI input and output power. The electromagnetic torque was estimated based on the model presented in [35,36].

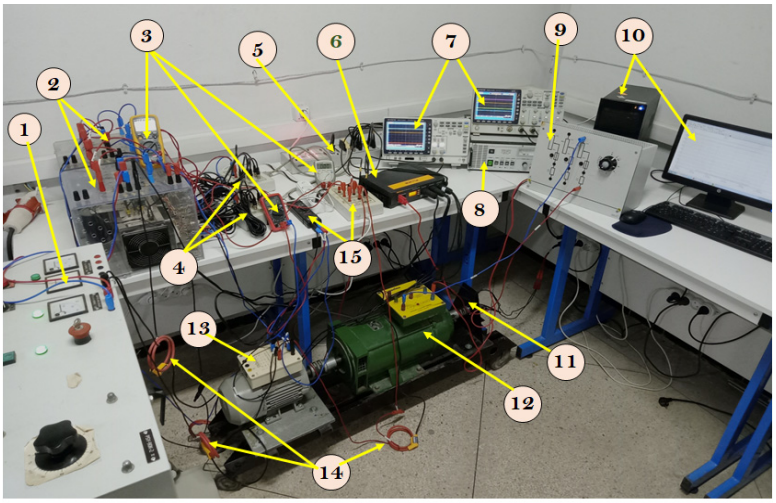

1-Three-phase power supply, 2-Dual inverters, 3-Multimeters, 4-Interface card, 5-Ds1104 control panel, 6-Power quality analyzer, 7-Oscilloscope, 8-DC power supply, 9-Variable resistive load, 10-Dspace1104, 11-Incremental encoder, 12-Mechanical DC load, 13-OEWIM, 14-Current sensors, 15-Voltage and current sensors.

Figure 10. Experimental prototype.

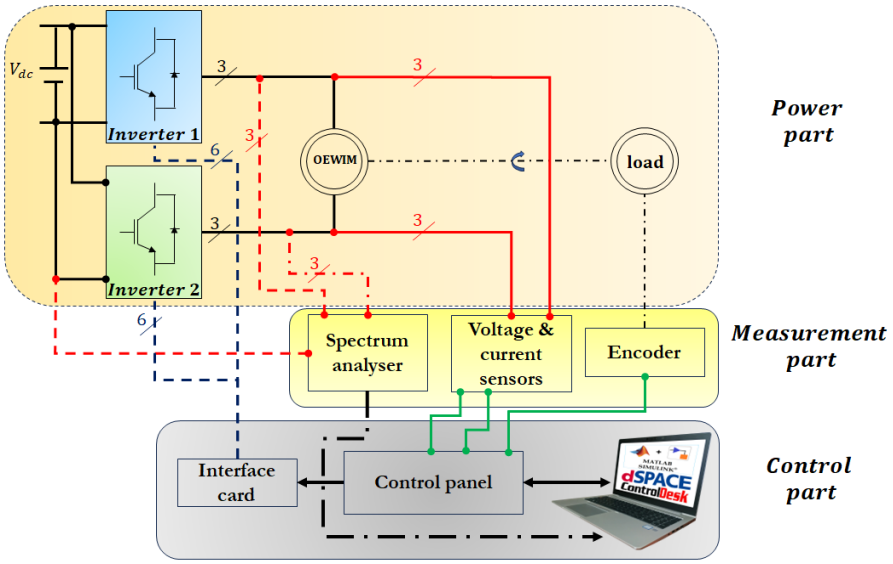

Figure 11. Flow chart of DI-OEWIM control implementation.

This test was designed to evaluate the overall performance of the OEWIM-DI system using different ASVPWM control techniques, and without any load torque. The results are shown in Figures 12–17, and a comprehensive summary of the data is given in Table 6.

Based on the results of this test, the following observations can be deduced:

- The ASVPWM2 strategies significantly improve voltage THD, reaching a value of 41.21%. The ASVPWM4 strategy stands out for its improvement in current THD, with a value of 14.03% (see Figure 13). These results are fully in line with those presented in Table 5 (Section 4).
- The ASVPWM1, ASVPWM3 and ASVPWM5 strategies generate five-level CMVs $\left(-\frac{V_{dc}}{2}; -\frac{V_{dc}}{6}; 0; \frac{V_{dc}}{6}; \frac{V_{dc}}{2}\right)$. In addition, they exhibit three-level ZSVs $\left(-\frac{V_{dc}}{3}; 0; \frac{V_{dc}}{3}\right)$, as illustrated in Figure 14a,c,e. These results correspond well to those presented in Figure 8, Table 5 (Section 4) and Table 4 (Section 3).
- In contrast, the ASVPWM2 and ASVPWM4 strategies generate four-level CMVs $\left(-\frac{V_{dc}}{2}; -\frac{V_{dc}}{6}; \frac{V_{dc}}{6}; \frac{V_{dc}}{2}\right)$, as shown in Figure 14b,d. However, they eliminate the ZSV completely due to the phase-shift angles $\theta_{DI} = 120°$ and $\theta_{DI} = 240°$. These results agree with those presented in Figure 8, Table 5 (Section 4) and Table 4 (Section 3).
- The ASVPWM2 and ASVPWM4 strategies stand out by minimizing total losses in the DI, with a percentage of 6.9%, compared with ASVPWM1 and ASVPWM5. In addition, they reduce total losses by 9.6% compared with ASVPWM3. These results are in agreement with those presented in Figure 9 and Table 5 (Section 4).
- The ASVPWM1 and ASVPWM5 techniques prove effective in reducing electromagnetic torque ripples, with values between 4.6 N.m and 9.8 N.m (see Figure 17). These results are in good agreement with those shown in Figure 10 and Table 5 (Section 4).

The experimental results justify the conclusions drawn in Section 4, shedding light on which technique offers appropriate performance. Indeed:

- The ASVPWM2 and ASVPWM4 strategies stand out for their significant improvement in voltage and current THD, as well as for their reduction in power losses with effective ZSV elimination.
- The ASVPWM1 and ASVPWM5 strategies show notable performance in terms of reduced power losses and improved torque variation.

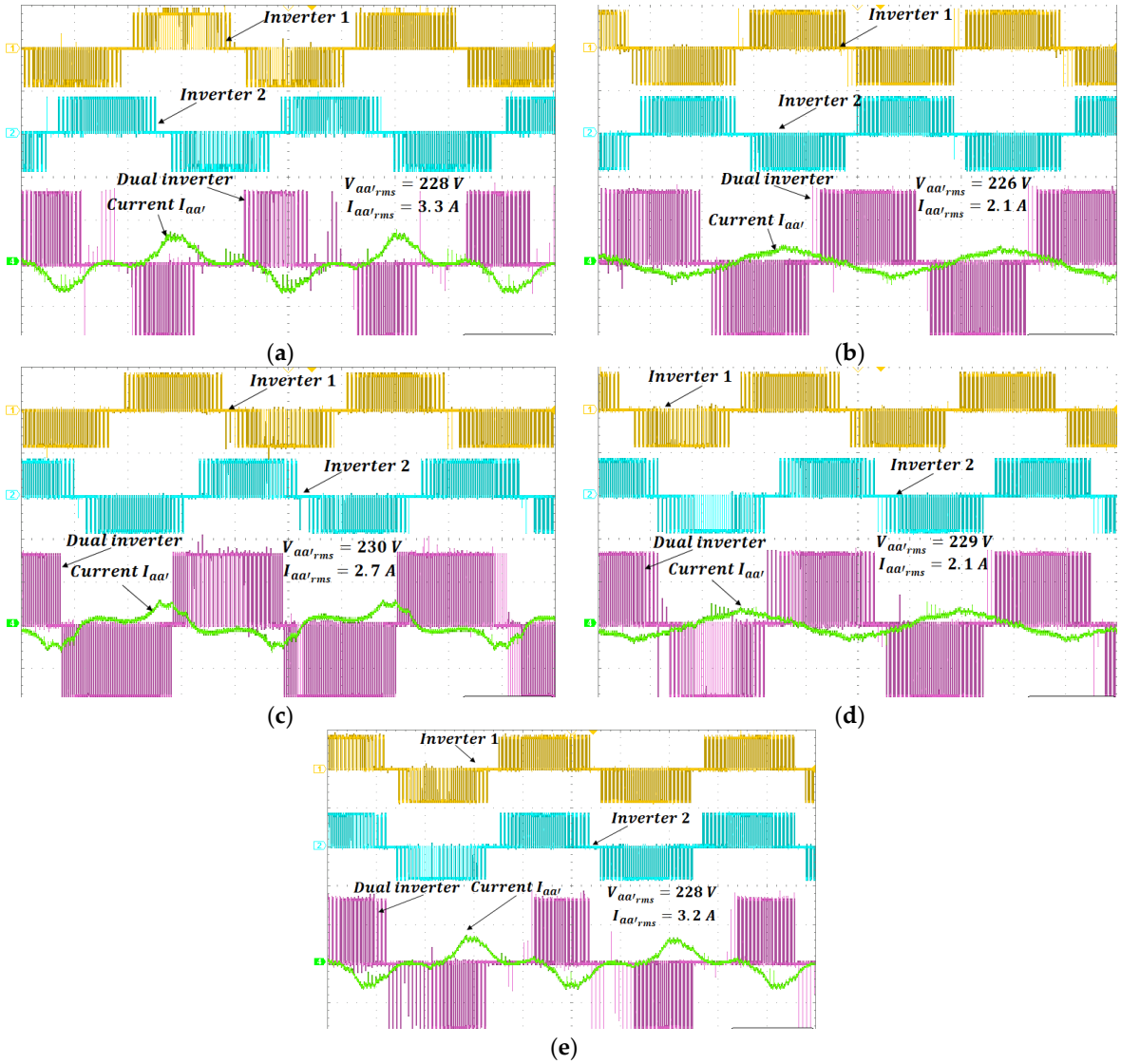

Figure 12. Experimental responses of the voltage of each inverter with the voltage and current of the OEWIM for different strategies: (**a**) ASVPWM1, (**b**) ASVPWM2, (**c**) ASVPWM3, (**d**) ASVPWM4, (**e**) ASVPWM5.

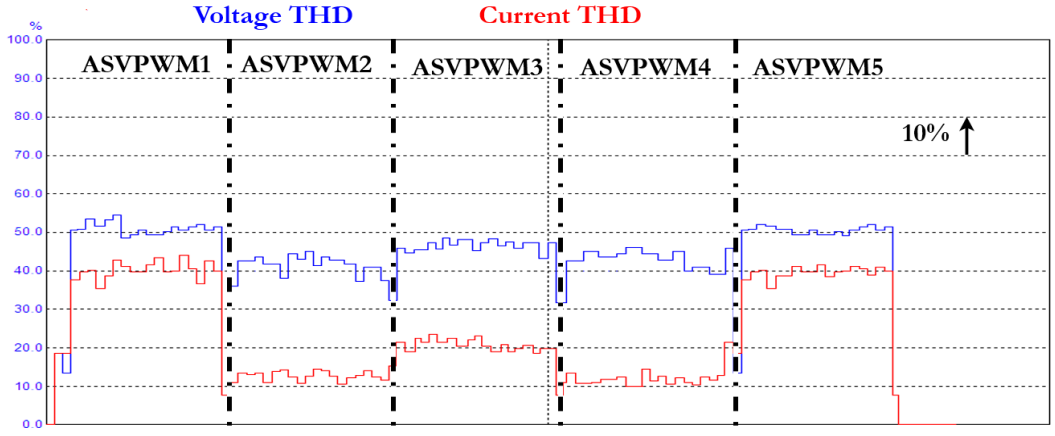

Figure 13. Experimental results of voltage and current THD of OEWIM with various ASVPWM strategies.

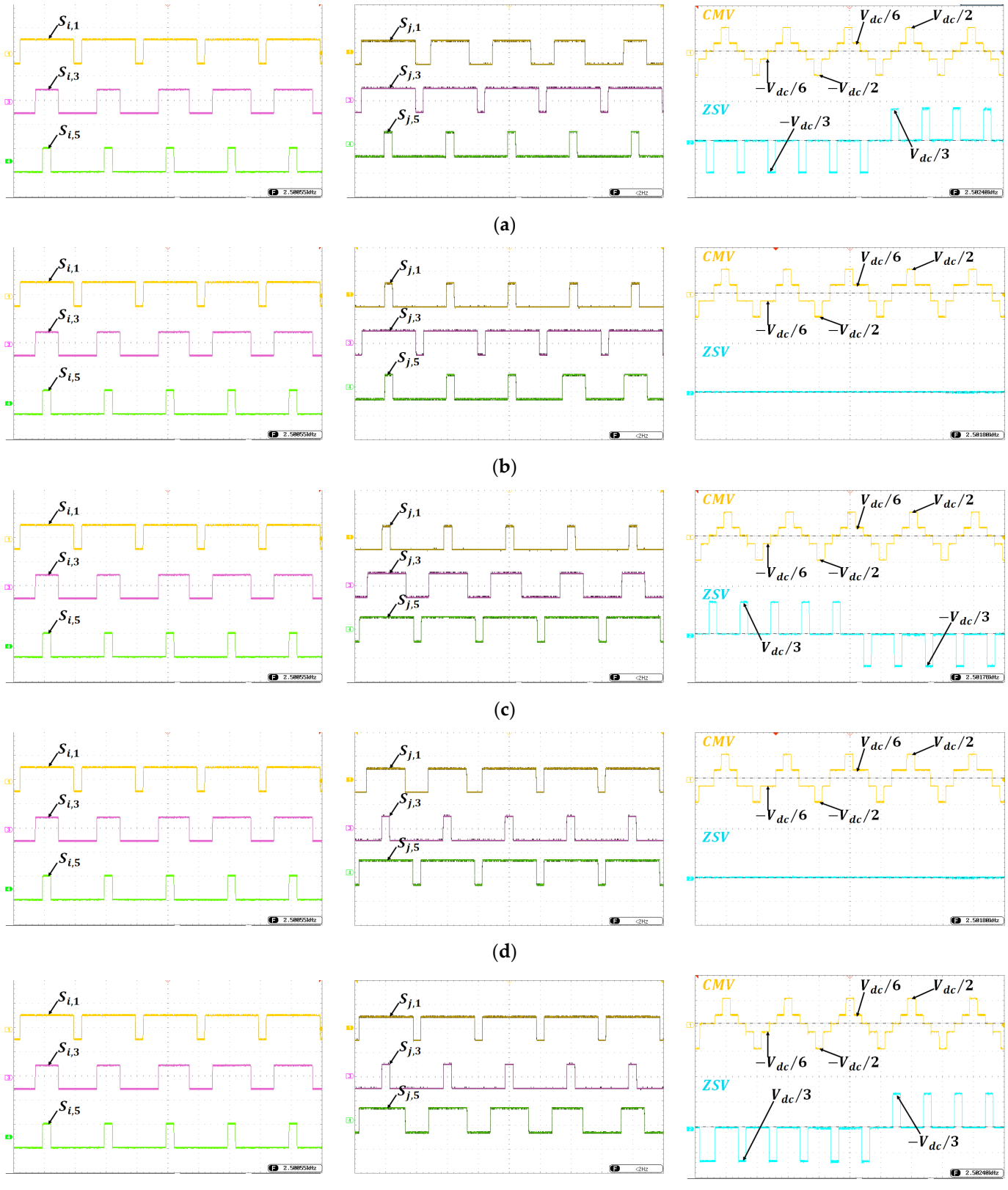

Figure 14. Switching states of inverter 1 (**left**), switching states of inverter 2 (**middle**) and the CMV with ZSV (**right**) of the strategies: (**a**) ASVPWM1, (**b**) ASVPWM2, (**c**) ASVPWM3, (**d**) ASVPWM4, (**e**) ASVPWM5.

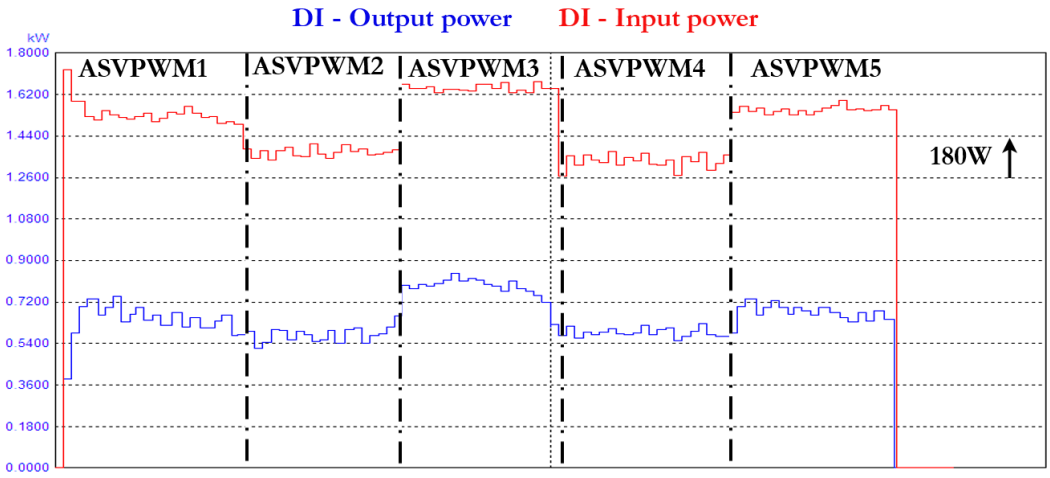

Figure 15. Experimental results of input and output power of DI with various ASVPWM strategies.

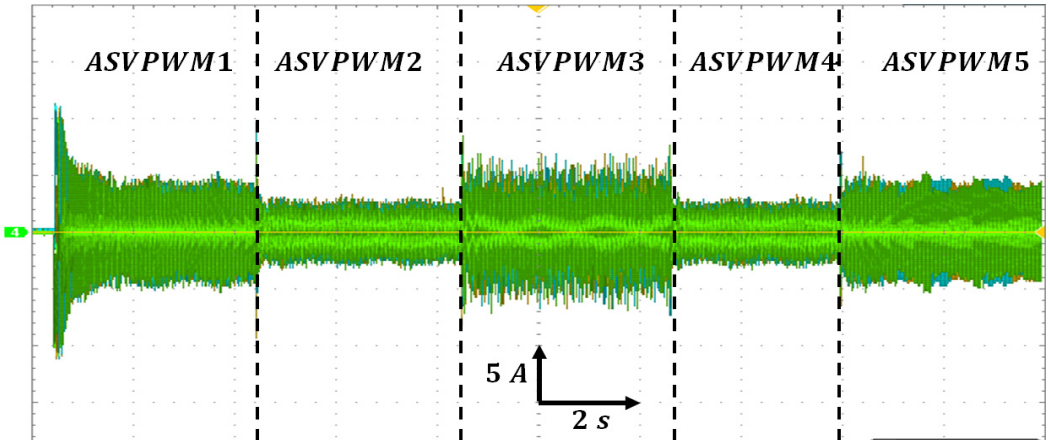

Figure 16. Experimental measurements of OEWIM currents using different ASVPWM strategies.

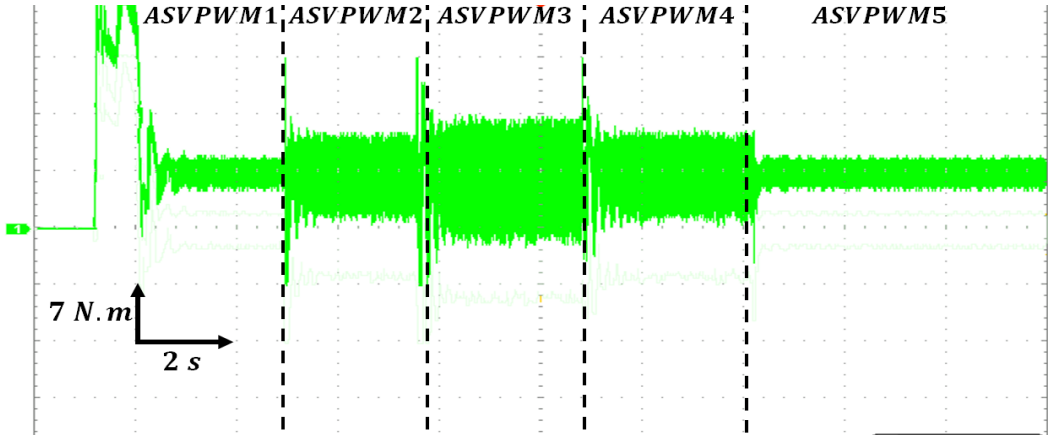

Figure 17. Experimental electromagnetic torque estimation as a function of ASVPWM strategies.

Table 6. Summary of experimental results.

Strategy	THD		Total Losses of DI [W]	Highest Level of CMV [V]	Highest Level of ZSV [V]	Torque Ripples T_e [N.m]
	V [%]	I [%]				
ASVPWM1	50.08	40.52	768	$\pm\frac{V_{dc}}{2}$	$\pm\frac{V_{dc}}{3}$	[4.6; 9.8]
ASVPWM2	41.21	14.03	715	$\pm\frac{V_{dc}}{2}$	0	[2.8; 11.5]
ASVPWM3	47.89	20.12	791	$\pm\frac{V_{dc}}{2}$	$\pm\frac{V_{dc}}{3}$	$[-1.4; 13.3]$
ASVPWM4	42.43	13.31	714	$\pm\frac{V_{dc}}{2}$	0	[2.8; 11.5]
ASVPWM5	50.36	40.43	767	$\pm\frac{V_{dc}}{2}$	$\pm\frac{V_{dc}}{3}$	[4.6; 9.8]

6. Conclusions

In this paper, we conducted a theoretical and experimental analysis to investigate the impact of Asymmetric Space Vector Pulse-Width Modulation (ASVPWM) strategy on the Dual-Inverter-fed Open-End Winding Induction Motor (DI-OEWIM) system powered by a common bus. The primary objective was to control a symmetrical system (DI-OEWIM) using various asymmetrical control techniques (ASVPWM). These techniques involved either basing or adding a shafted angle between the reference voltages of the two inverters, while assessing their effects on the overall performance of the system, including Total Harmonic Distortion (THD), power losses, Common Mode Voltage (CMV), Zero-Sequence Voltage (ZSV), shafted angle and electromagnetic torque ripples.

The analysis of experimental and simulation results yielded several significant conclusions:

- The application of an asymmetrical control strategy influenced effectively the behavior of the DI-OEWIM system.
- Choosing the appropriate ASVPWM control strategy presents a dilemma, necessitating thorough evaluation to achieve optimal system performance.
- Based on the findings, we give preference to the ASVPWM2 and ASVPWM4 strategies, which not only effectively eliminate ZSV, but also improve current THD by 65% and voltage THD by 17%. What is more, they reduce DI losses by 6% compared to the ASVPWM1 and ASVPWM5 strategies.

Consequently, building upon the promising outcomes of this study, our future objective is to refine the ASVPWM strategies to enhance the performance of the OEWIM-DI system in the following ways:

- We plan to employ optimization techniques aimed at adjusting the phase-shift angle between the two inverters to optimize the overall performance of our system.
- For the ASVPWM2 and ASPVWM4 strategies, we propose implementing discontinuous D-ASVPWM so that the losses are reduced and the system efficiency is improved.

Author Contributions: Methodology, H.C. and S.A.E.M.A.; software, M.Z. and S.A.E.M.A.; validation, M.Z. and S.A.E.M.A.; investigation, S.A.E.M.A.; resources, S.A.E.M.A.; writing—original draft preparation, M.Z. and S.A.E.M.A.; writing—review and editing, H.C.; supervision, H.C. and S.A.E.M.A. All authors have read and agreed to the published version of the manuscript.

Funding: This research received no external funding.

Data Availability Statement: Data are contained within the article.

Conflicts of Interest: The authors declare no conflict of interest.

Appendix A

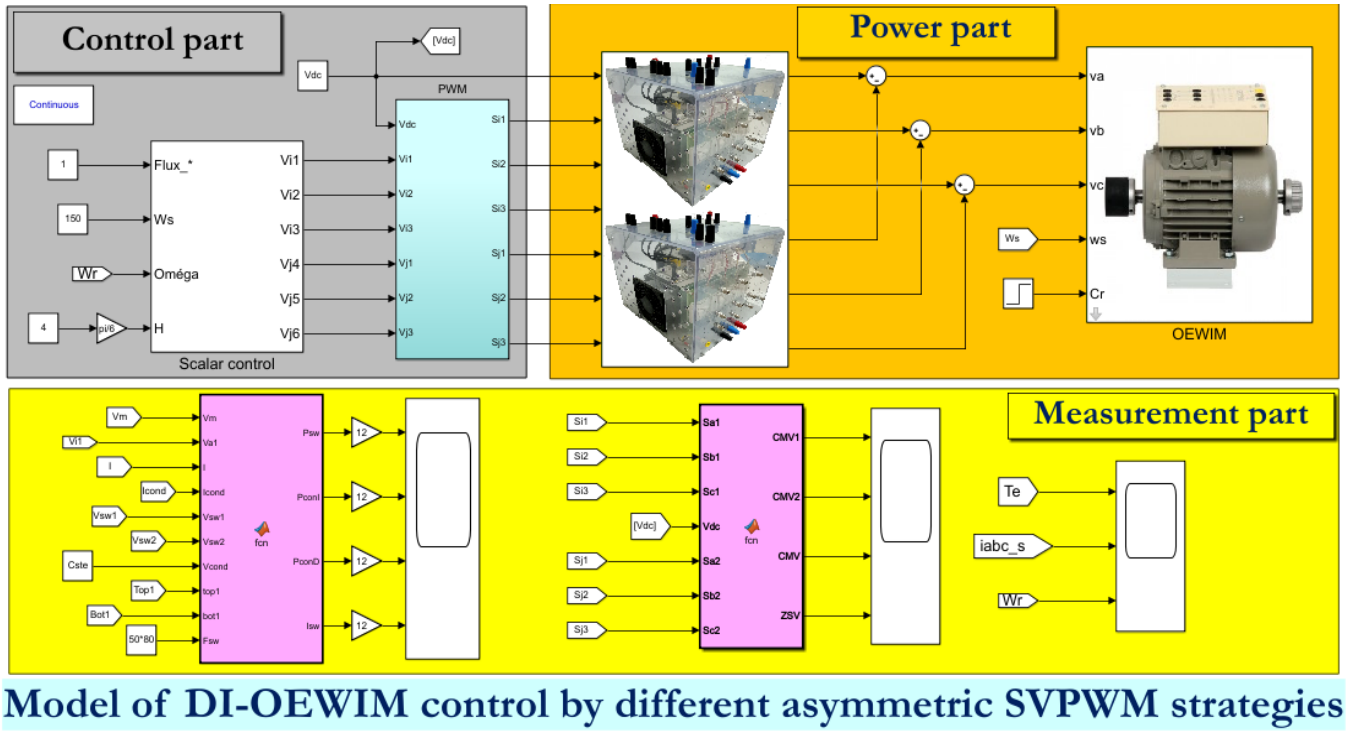

Figure A1. Simulation model of the ASVPWM control for OEWIM.

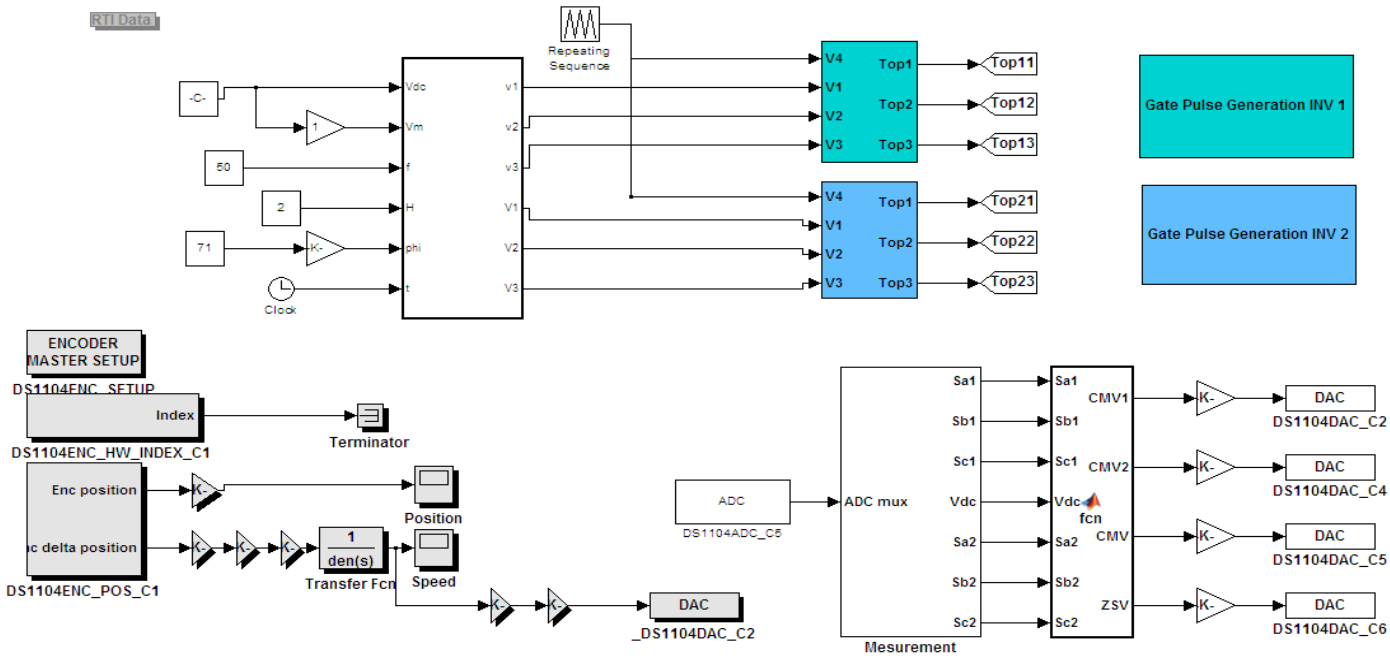

Figure A2. Model of ASVPWM strategies under Matlab/Simulink and DS1104 environment.

Appendix B

Table A1. DI-OEWIM parameters.

Parameter	Symbol	Value	Unit
Rated power	P_n	1500	[W]
Rated voltage	U_n; V_n	230; 400	[V]
Full load current	J_n; I_n	5.7; 3.3	[A]
Frequency	F	50	[Hz]
Stator resistance	R_s	3.93	[Ω]
Stator inductance	L_s	0.3374	[H]
Rotor resistance	R_r	3.5349	[Ω]
Rotor leakage inductance	L_r	0.3374	[H]
Magnetizing inductance	L_m	0.3243	[H]
Power factor	$\cos\varphi$	0.77	--
Poles number	P	2	--
Moment of inertia	J	0.01643	$\left[\mathrm{N.m(rad/s)}^{-1}\right]$
Friction coefficient	f	0.00138	$\left[\mathrm{Kg.m}^2/\mathrm{s}\right]$
Rated torque	C_n	10.0167	[N.m]

References

1. Ibrahim, N.F.; Ardjoun, S.A.E.M.; Alharbi, M.; Alkuhayli, A.; Abuagreb, M.; Khaled, U.; Mahmoud, M.M. Multiport Converter Utility Interface with a High-Frequency Link for Interfacing Clean Energy Sources (PV\Wind\Fuel Cell) and Battery to the Power System: Application of the HHA Algorithm. *Sustainability* **2023**, *15*, 13716. [CrossRef]
2. Mahmoud, M.M.; Atia, B.S.; Esmail, Y.M.; Ardjoun, S.A.E.M.; Anwer, N.; Omar, A.I.; Alsaif, F.; Alsulamy, S.; Mohamed, S.A. Application of Whale Optimization Algorithm Based FOPI Controllers for STATCOM and UPQC to Mitigate Harmonics and Voltage Instability in Modern Distribution Power Grids. *Axioms* **2023**, *12*, 420. [CrossRef]
3. Ardjoun, S.A.E.M.; Abid, M.; Aissaoui, A.G.; Tahour, A. A Robust Sliding Mode Control Applied To The Double Fed Induction Machine. *IU-J. Electr. Electron. Eng.* **2013**, *12*, 1445–1451.
4. Miloudi, H.; Miloudi, M.; Ardjoun, S.A.E.M.; Mahmoud, M.M.; Telba, A.A.; Denaï, M.; Khaled, U.; Ewias, A.M. Electromagnetic Compatibility Characterization of Start-Capacitor Single-Phase Induction Motor. *IEEE Access* **2024**, *12*, 2313–2326. [CrossRef]
5. Subotic, I.; Bodo, N.; Levi, E.; Jones, M. Onboard Integrated Battery Charger for EVs Using an Asymmetrical Nine-Phase Machine. *IEEE Trans. Ind. Electron.* **2015**, *62*, 3285–3295. [CrossRef]
6. Dehghani kiadehi, A.; Drissi, K.E.K.; Pasquier, C. Angular Modulation of Dual-Inverter Fed Open-End Motor for Electrical Vehicle Applications. *IEEE Trans. Power Electron.* **2016**, *31*, 2980–2990. [CrossRef]
7. Bojoi, R.; Cavagnino, A.; Tenconi, A.; Vaschetto, S. Control of Shaft-Line-Embedded Multiphase Starter/Generator for Aero-Engine. *IEEE Trans. Ind. Electron.* **2016**, *63*, 641–652. [CrossRef]
8. Sun, C.; Ai, S.; Hu, L.; Chen, Y. The Development of a 20MW PWM Driver for Advanced Fifteen-Phase Propulsion Induction Motors. *J. Power Electron.* **2015**, *15*, 146–159. [CrossRef]
9. Huang, Z.; Yang, T.; Giangrande, P.; Galea, M.; Wheeler, P. Technical Review of Dual Inverter Topologies for More Electric Aircraft Applications. *IEEE Trans. Transp. Electrif.* **2022**, *8*, 1966–1980. [CrossRef]
10. Muduli, U.R.; Beig, A.R.; Behera, R.K.; Jaafari, K.A.; Alsawalhi, J.Y. Predictive Control with Battery Power Sharing Scheme for Dual Open-End-Winding Induction Motor Based Four-Wheel Drive Electric Vehicle. *IEEE Trans. Ind. Electron.* **2022**, *69*, 5557–5568. [CrossRef]
11. Hong, J.; Lee, H.; Nam, K. Charging method for the secondary battery in dual-inverter drive systems for electric vehicles. *IEEE Trans. Power Electron.* **2015**, *30*, 909–921. [CrossRef]
12. Rovere, L.; Formentini, A.; Calzo, G.L.; Zanchetta, P.; Cox, T. Zero sequence voltage elimination for dual-fed common DC-link open-end winding PMSM high-speed starter–generator—Part I: Modulation. *IEEE Trans. Ind. Appl.* **2019**, *55*, 7804–7812. [CrossRef]
13. Rovere, L.; Formentini, A.; Calzo, G.L.; Zanchetta, P.; Cox, T. Zero sequence voltage elimination for dual-fed common DC link open-end winding PMSM high-speed starter-generator—Part II: Deadtime hysteresis control of zero-sequence current. *IEEE Trans. Ind. Appl.* **2019**, *55*, 7813–7821. [CrossRef]

14. Kodumur Meesala, R.E.; Kunisetti, V.P.K.; Kumar Thippiripati, V. Enhanced Predictive Torque Control for Open End Winding Induction Motor Drive Without Weighting Factor Assignment. *IEEE Trans. Power Electron.* **2019**, *34*, 503–513. [CrossRef]
15. Lakhimsetty, S.; Satelli, V.S.P.; Rathore, R.S.; Somasekhar, V.T. Multilevel Torque Hysteresis-Band Based Direct-Torque Control Strategy for a Three-Level Open-End Winding Induction Motor Drive for Electric Vehicle Applications. *IEEE J. Emerg. Sel. Topics Power Electron.* **2019**, *7*, 1969–1981. [CrossRef]
16. Srinivas, S.; Ramachandra Sekhar, K. Theoretical and Experimental Analysis for Current in a Dual-Inverter-Fed Open-End Winding Induction Motor Drive with Reduced Switching PWM. *IEEE Trans. Ind. Electron.* **2013**, *60*, 4318–4328. [CrossRef]
17. Huang, Z.; Yang, T.; Giangrande, P.; Chowdhury, S.; Galea, M.; Wheeler, P. Enhanced performance of dual inverter with a floating capacitor for motor drive applications. *IEEE Trans. Power Electron.* **2020**, *36*, 6903–6916. [CrossRef]
18. Chowdhury, S.; Wheeler, P.W.; Patel, C.; Gerada, C. A multilevel converter with a floating bridge for open-end winding motor drive applications. *IEEE Trans. Ind. Electron.* **2016**, *63*, 5366–5375. [CrossRef]
19. Reddy, B.V.; Somasekhar, V.T.; Kalyan, Y. Decoupled Space-Vector PWM Strategies for a Four-Level Asymmetrical Open-End Winding Induction Motor Drive with Waveform Symmetries. *IEEE Trans. Ind. Electron.* **2011**, *58*, 5130–5141. [CrossRef]
20. Somasekhar, V.T.; Srinivas, S.; Kumar, K.K. Effect of Zero-Vector Placement in a Dual-Inverter Fed Open-End Winding Induction-Motor Drive With a Decoupled Space-Vector PWM Strategy. *IEEE Trans. Ind. Electron.* **2008**, *55*, 2497–2505. [CrossRef]
21. Kiadehi, A.D.; Drissi, K.E.K.; Pasquier, C. Voltage THD Reduction for Dual-Inverter Fed Open-End Load With Isolated DC Sources. *IEEE Trans. Ind. Electron.* **2017**, *64*, 2102–2111. [CrossRef]
22. Chen, S.; Lipo, T.A.; Fitzgerald, D. Source of induction motor bearing currents caused by PWM inverters. *IEEE Trans. Energy Convers.* **1996**, *11*, 25–32. [CrossRef]
23. Zhong, E.; Lipo, T.A. Improvements in EMC performance of inverter-fed motor drives. *IEEE Trans. Ind. Appl.* **1995**, *31*, 1247–1256. [CrossRef]
24. Kalaiselvi, J.; Srinivas, S. Bearing Currents and Shaft Voltage Reduction in Dual-Inverter-Fed Open-End Winding Induction Motor with Reduced CMV PWM Methods. *IEEE Trans. Ind. Electron.* **2015**, *62*, 144–152. [CrossRef]
25. Zerdani, M.; Ardjoun, S.E.; Chafouk, H.; Denai, M. Experimental Validation of a New Power Chain for Electric Vehicles. In Proceedings of the 2022 2nd International Conference on Innovative Research in Applied Science, Engineering and Technology (IRASET), Meknes, Morocco, 3–4 March 2022; pp. 1–6.
26. Mohammed, Z.; Mehdi, A.S.A.E.; Houcine, C.; Mouloud, D. Experimental Analysis of the Decoupled PWM Influence on the Open-End Winding Induction Machine. In Proceedings of the 2022 2nd International Conference on Advanced Electrical Engineering (ICAEE), Constantine, Algeria, 29–31 October 2022; pp. 1–5.
27. Zerdani, M.; Ardjoun, S.A.E.M.; Chafouk, H.; Denaï, M. Experimental Investigation of Decoupled Discontinuous PWM Strategies in Open-End Winding Induction Motor Supplied by a Common DC-Link. *IEEE J. Emerg. Sel. Top. Power Electron.* **2023**, *11*, 3087–3096. [CrossRef]
28. Lakhimsetty, S.; Somasekhar, V.T. A four-level open-end winding induction motor drive with a nested rectifier–inverter combination with two DC power supplies. *IEEE Trans. Power Electron.* **2019**, *34*, 8894–8904. [CrossRef]
29. Lakhimsetty, S.; Somasekhar, V.T. An Efficient Predictive Current Control Strategy for a Four-Level Open-End Winding Induction Motor Drive. *IEEE Trans. Power Electron.* **2020**, *35*, 6198–6207. [CrossRef]
30. Sun, D.; Zheng, Z.; Lin, B.; Zhou, W.; Chen, M. A hybrid PWM-based field weakening strategy for a hybrid-inverter-driven open winding PMSM system. *IEEE Trans. Energy Convers.* **2017**, *32*, 857–865. [CrossRef]
31. Dong, Z.; Song, Z.; Wang, W.; Liu, C. Improved Zero-Sequence Current Hysteresis Control-Based Space Vector Modulation for Open End Winding PMSM Drives with Common DC Bus. *IEEE Trans. Ind. Electron.* **2023**, *70*, 10755–10760. [CrossRef]
32. Baranwal, R.; Basu, K.; Mohan, N. Carrier-based implementation of SVPWM for dual two-level VSI and dual matrix converter with zero common-mode voltage. *IEEE Trans. Power Electron.* **2015**, *30*, 1471–1487. [CrossRef]
33. Somasekhar, V.T.; Gopakumar, K.; Shivakumar, E.G.; Petit, A. Multi-level voltage space phasor generation for an open-end winding induction motor drive using a dual inverter scheme with asymmetrical DC-link voltages. *EPE J.* **2009**, *12*, 59–77. [CrossRef]
34. Holmes, D.G.; Lipo, T.A. *Pulse Width Modulation for Power Converters: Principles and Practice*; John Wiley & Sons: Hoboken, NJ, USA, 2003.
35. Younes, D.; Ahmed El Mehdi, A.S.; Houcine, C.; Mouloud, D. Sensorless Torque Control of an Electric Vehicle Driven by an Open End Winding Induction Motor: An Experimental Study. In Proceedings of the 2023 Second International Conference on Energy Transition and Security (ICETS), Adrar, Algeria, 12–14 December 2023; pp. 1–6.
36. Younes, D.; Ahmed El Mehdi, A.S.A.; Mouloud, D.; Houcine, C. Real-Time Implementation of the Luenberger Torque Observer for an Induction Motor. In Proceedings of the 2023 2nd International Conference on Electronics, Energy and Measurement (IC2EM), Medea, Algeria, 28–29 November 2023; pp. 1–4.